DOE/ER/03518-94

MASTER

THE STUDY OF DEFECTS, RADIATION DAMAGE AND IMPLANTED GASES IN SOLIDS BY FIELD-ION AND ATOM-PROBE MICROSCOPY

by

David N. Seidman, Jun Amano and Alfred Wagner

Cornell University
Ithaca, New York 14853

DISCLAIMER

This book was prepared as an account of work sponsored by an agency of the United States Government. Neither the United States Government nor any agency thereof, nor any of their employees, makes any warranty, express or implied, or assumes any legal liability or responsibility for the accuracy, completeness, or usefulness of any information, apparatus, product, or process disclosed, or represents that its use would not infringe privately owned rights. Reference herein to any specific commercial product, process, or service by trade name, trademark, manufacturer, or otherwise, does not necessarily constitute or imply its endorsement, recommendation, or favoring by the United States Government or any agency thereof. The views and opinions of authors expressed herein do not necessarily state or reflect those of the United States Government or any agency thereof.

October 1980

Report #4323

Issued by

The Materials Science Center

Prepared for

The U.S. Department of Energy under Contract No. DE-AC02-76ER03158.

E#B

DISTRIBUTION OF THIS DOCUMENT IS UNLIMITED

DISCLAIMER

This report was prepared as an account of work sponsored by an agency of the United States Government. Neither the United States Government nor any agency Thereof, nor any of their employees, makes any warranty, express or implied, or assumes any legal liability or responsibility for the accuracy, completeness, or usefulness of any information, apparatus, product, or process disclosed, or represents that its use would not infringe privately owned rights. Reference herein to any specific commercial product, process, or service by trade name, trademark, manufacturer, or otherwise does not necessarily constitute or imply its endorsement, recommendation, or favoring by the United States Government or any agency thereof. The views and opinions of authors expressed herein do not necessarily state or reflect those of the United States Government or any agency thereof.

DISCLAIMER

Portions of this document may be illegible in electronic image products. Images are produced from the best available original document.

THE STUDY OF DEFECTS, RADIATION DAMAGE AND IMPLANTED GASES IN SOLIDS BY FIELD-ION AND ATOM-PROBE MICROSCOPY†

David N. Seidman,* Jun Amano** and Alfred Wagner‡

Cornell University, Department of Materials Science and Engineering and the Materials Science Center, Bard Hall, Ithaca, New York 14853 U.S.A.

The ability of the field-ion microscope to image individual atoms has been applied, at Cornell University, to the study of fundamental properties of point defects in irradiated or quenched metals. The capability of the atom probe field-ion microscope to determine the chemistry — that is, the mass-to-charge ratio — of a *single* ion has been used to investigate the behavior of different implanted species in metals. A brief review is presented of: (1) the basic physical principles of the field-ion and atom-probe microscopes; (2) the many applications of these instruments to the study of defects and radiation damage in solids; and (3) the application of the atom-probe field-ion microscope to the study of the behavior of implanted ^{3}He and ^{4}He atoms in tungsten. The paper is heavily referenced so that the reader can pursue his specific research interests in detail.

† This work was supported by the U.S. Department of Energy. Additional support was received from the National Science Foundation through the use of the technical facilities of the Materials Science Center at Cornell University.

* John Simon Guggenheim Memorial Foundation Fellow 1980-81.

** Now at Hewlett-Packard Laboratories, 1501 Page Mill Rd., Palo Alto, CA 94304

‡ Now at Bell Laboratories, 600 Mountain Avenue, Murray Hill, NJ 07974

Introduction

In this paper an attempt is made to introduce the reader to some of the basic physical ideas involved in the field-ion and atom-probe field-ion microscope (FIM) techniques (see section on General Background Material), and to the applications of these techniques to the study of defects and radiation damage in solids (see section following the first one). The final section discusses, in precis form, the application of the atom-probe FIM to the study of the behavior of implanted ^{3}He and ^{4}He atoms in tungsten. The paper is heavily referenced so that the reader can pursue his specific research interests in detail.

General Background Material

The invention of the FIM and the atom-probe FIM by Müller (1,2) has provided the experimentalist with tools which allow both the direct observation of all the common defects (point, line, planar and precipitates) on an atomic scale and also the simultaneous determination of chemical effects on an atomic scale (the minimum detectable mass is equal to the mass of a *single atom*).

The atomic structure of the lattice is observed for those atoms which lie on the surface of a sharply pointed (~200 to 500Å in diameter) FIM specimen; the area imaged is $\sim 10^{-10}$ to 10^{-11}cm^2. The information concerning the positions of the atoms is carried to a phosphor screen or a channel electron multiplier array (3,4) by an imaging gas which is typically helium or neon. The imaging gas atoms are ionized, by a tunneling mechanism, in the high local electric fields (~4.5 V Å^{-1} to ionize a helium atom) that exist at the site of individual atoms as a result of a positive potential applied to a sharply pointed FIM specimen (5). The positively-charged ions are repelled from the sharply-pointed specimen and then travel along the electric field lines to the phosphor screen which is at earth potential (see Figure 1); typically the phosphor screen is at a distance of between 4 to 10 cm from the FIM specimen. The image formed of the atoms on the surface of the FIM specimen, in the above manner, constitutes a point projection image with sufficient magnification to resolve individual atoms.

The interior of the specimen can be examined employing the field-evaporation process. The latter process consists of increasing the electric field to a value such that the potential energy curve for an ion on the surface of the specimen (this statement assumes that the state in which the metal atoms exist on the surface of the specimen is the ionic state) is deformed by the applied field to form a Schottky hump (6). The ions then evaporate (or sublime) by either jumping over this small Schottky hump as a result of a thermally-activated step or by tunneling through it; this process is called field evaporation or field desorption in the case of a solute atom. The field evaporation process can be controlled — with great precision — by applying the positive potential in the form of short (1 to 10 msec in width) high-voltage pulses. This latter technique is called pulse field evaporation; it is possible by this technique to dissect an atomic plane by removing one to two atoms per pulse. Thus, the atoms contained within the interior of the specimen can be imaged, albeit at the surface, at a rate which is determined by the experimentalist. In practice one can examine $\approx 10^{-16}$ to 10^{-17}cm^3 of material, during the course of one afternoon, via the pulse field evaporation technique. At Cornell we have developed semi-automated techniques for the process of applying the field evaporation pulse in conjunction with the simultaneous recording of large numbers of frames of 35 cine film [(15 to 30)$\times 10^3$ frames per day] as well as developing techniques for the scanning of this film (7). It is clear, with the advantage of hindsight, that these two steps were essential to the successful application of the FIM technique to problems in the field of radiation damage.

The invention (2) of the time-of-flight (TOF) atom-probe FIM has provided the materials scientist with a unique instrument for the study of the interaction of impurity atoms or alloying elements with point, line or planar defects. The TOF atom-probe FIM (hereafter called an atom probe) consists of an FIM combined with a special TOF mass spectrometer (see Figure 1). This spectrometer allows the investigator to identify chemically any atom that appears in an FIM image. Thus, it is now possible to both image the microstructural features of a specimen and to measure the mass-to-charge ratio (m/n) of individual ions from preselected regions of a specimen with a lateral spatial resolution (i.e., within the surface) of a few angstroms and a depth spatial resolution that is determined by the interplanar spacing; the latter quantity can be tenths of an angstrom for a high index plane. An atom probe with a straight TOF tube has a mass-resolution ($m/\Delta m$) of ~200 while an atom probe with a Poschenrieder lens (8) has an $m/\Delta m$ value of >1000 (9).

Figure 1 exhibits a schematic diagram that illustrates the main features of our straight TOF atom probe. A specimen with a radius of 50 to 500Å is maintained at a positive potential (3-20 kV) so that gas atoms surrounding the specimen are ionized over individual atomic sites and are projected radially outward to produce a visual image on the internal-image-intensification system. When a short high-voltage pulse is applied, atoms on the surface of the specimen are field evaporated in the form of ions. Those ions projected into the probe hole at the center of the internal-image-intensification system pass down the flight tube to the chevron ion detector. The TOFs of the ions and the voltages applied to the specimen are measured and the (m/n) ratios are calculated employing the equation:

$$m/n = 2e(V_{dc} + \alpha V_{pulse})\,(t-t_o)^2/d^2;$$

where e is the charge on an electron, V_{dc} the steady-state imaging voltage, V_{pulse} the pulse evaporation voltage, α the so-called pulse factor, d the flight distance, and $(t-t_0)$ the actual TOF of the ion. The quantity t is the observed TOF and t_o is the total delay time. The procedure we have developed to determine (m/n) is based on making V_{pulse} a constant fraction of V_{dc}; i.e., $V_{pulse} = fV_{dc}$ where f is a constant that is usually in the range 0.05 to 0.25 — the exact value depends on the specific alloy being analyzed. By the controlled pulse field evaporation of successive atomic layers it is possible to examine the bulk of the specimen and to reconstruct in three dimensions the correspondence between special microstructural features and chemical composition.

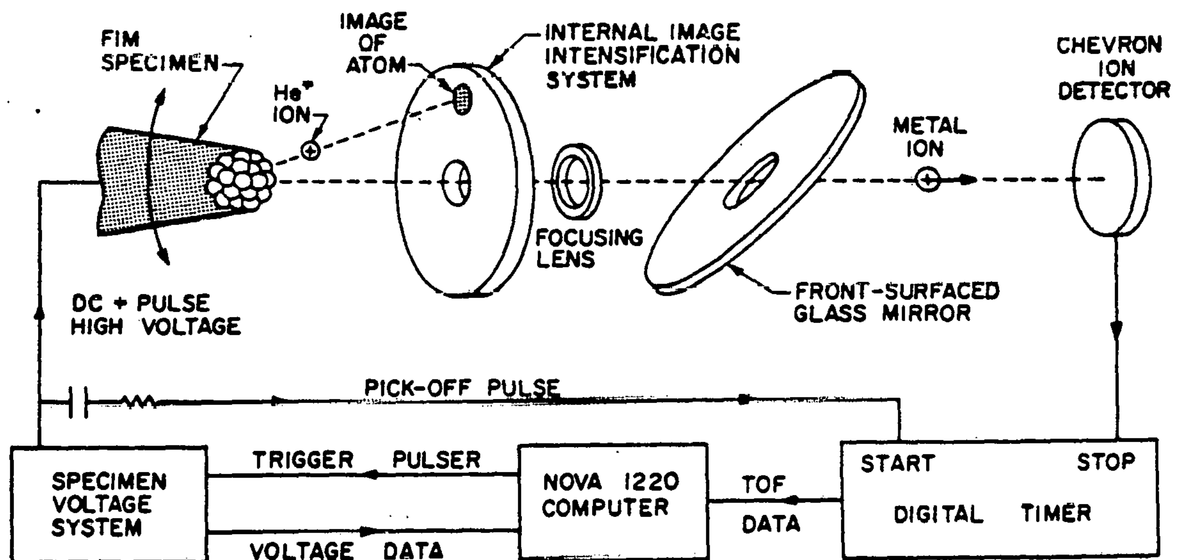

Fig. 1 Schematic diagram of the TOF atom-probe FIM. Shown at the top are the internal elements of the atom-probe including the FIM specimen, the internal-image-intensification system, the focusing lens, the 45° glass mirror, and the Chevron ion-detector. As indicated in the lower part of the figure, the specimen voltage system and the digital timer of the TOF mass spectrometer are operated automatically by a Nova 1220 minicomputer.

The details of the atom-probe are now summarized. The specimen is mounted on a liquid-helium-cooled goniometer stage which provides rotation about two orthogonal axes, thus allowing any portion of the specimen's surface to be projected into the probe hole for mass analysis. The goniometer stage is also translatable in three mutually orthogonal directions to facilitate alignment of the specimen with respect to the probe hole. The specimen is cooled by liquid helium in order to improve the quality of the FIM image and control the diffusivity of point defects; the temperature of the specimen is variable continuously from 13 to 450 K. The specimen is inserted into the goniometer stage via a high-vacuum ($<10^{-6}$ torr) specimen exchange device which allows rapid transfer of specimens without breaking the vacuum in the FIM. The specimen can also be irradiated *in-situ* with low energy gas ions (100 eV to ~ 5 keV) employing a specially constructed ion-gun.

The internal-image-intensification system consists of a 75 mm diameter channel-electron-multiplier array (CEMA) and a phosphor screen with 5 mm diameter holes through their centers. The distance from the FIM specimen to the front surface of the internal-image-intensification system is continuously variable so that the magnification of the FIM image, as well as the size of the region projected onto the probe hole, can be varied by an areal magnification factor of ~64X. An electrostatic lens immediately behind the internal-image-intensification system serves to focus those ions which pass through the probe hole down to a 1 mm diameter spot on the ion detector at the end of a 2.22 m long flight tube. The ion detector consists of two CEMAs placed in series in the Chevron configuration and a phosphor screen which provides a visual image of the ion beam. The atom probe was constructed to operate routinely in ultra-high vacuum ($\lesssim 5 \times 10^{-10}$ Torr) in order to minimize the interaction of residual gas atoms with the specimen.

The mass-spectrometer electronics, consisting of the specimen-voltage system and the digital timer are operated by a Nova 1220 minicomputer. This computerized system can automatically analyze up to 600 TOF events min^{-1} so that statistically significant results can be readily obtained even for small solute concentrations. As shown in the lower part of Figure 1 the computer triggers the V_{pulse} to the specimen which causes atoms on the surface of the specimen to be field-evaporated. A fraction of V_{pulse} is picked off and used to start an eight-channel digital timer which has a ± 10 nsec resolution. The pulses produced when ions strike the detector are used to stop the timer. A total of eight ion species from a single evaporation event can be identified. The controls of the dc and pulse power supplies, as well as the power supply for the focusing lens, are coupled so that the pulse and lens voltages are maintained at a constant fraction of the dc voltage. The values of V_{dc} and V_{pulse} applied to the specimen are measured by an analog-to-digital converter and read into the computer along with the TOF data. The (m/n) ratios are calculated by the computer and stored in the computer memory in the form of a histogram of the number of events versus m/n. In addition, the TOF and voltage data are stored on floppy discs so that the results of the run can be re-analyzed in the future. The computer is interfaced to a Tektronix 4010 graphics display terminal and Tektronix hard copy unit (not shown in Figure 1) so that a hard copy of the histogram can be obtained in ~20 sec.

Three examples that illustrate the resolving power of our instrument are shown in Figures 2 and 3. Figure 2 exhibits the seven stable isotopes of molybdenum in the plus-two charge state; note that the isotopes are readily distinguished from one another. The peaks associated with the five stable isotopes of tungsten are also readily distinguished in the W^{+3} spectrum shown in Figure 3a. For comparison Figure 3b exhibits the stable isotopes of tungsten and rhenium in the plus-three charge state; this spectrum was obtained from a specimen with a nominal composition of W-25 at.% Re. The concentration of rhenium in the W-25 at.% Re alloy was determined by atom-probe analysis to be 22 ± 2 at.% and there was no apparent segregation or clustering of rhenium. The case of the tungsten-rhenium alloy is a worst case situation, for this instrument, as it requires a mass resolution approaching 200.

Additional material concerning the FIM and atom-probe techniques and their applications can be found in reference numbers (5, 10-17). The work performed at Cornell in the fields of defect physics and radiation damage has been summarized in detail in several review articles (18-21). For technical details concerning the computer controlled atom probe we have constructed at Cornell, see reference numbers (22-26).

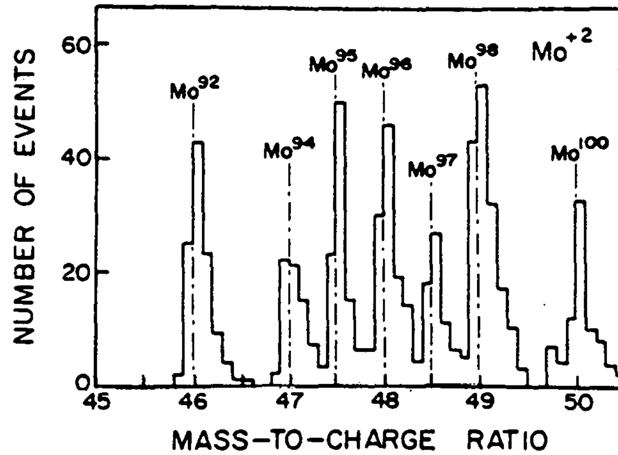

Fig. 2 Spectrum of Mo^{+2} obtained at a background pressure of 5×10^{-9} Torr, a specimen temperature of ~60 K and with the probe hole in the internal-image-intensification system near the (110) pole. The pulse fraction (f) was 0.025 and the calibration parameters used were $\alpha=1.482$, $t_o=0.56\mu$sec, and d=2.213 m. The total number of Mo^{+2} events in this histogram is 696.

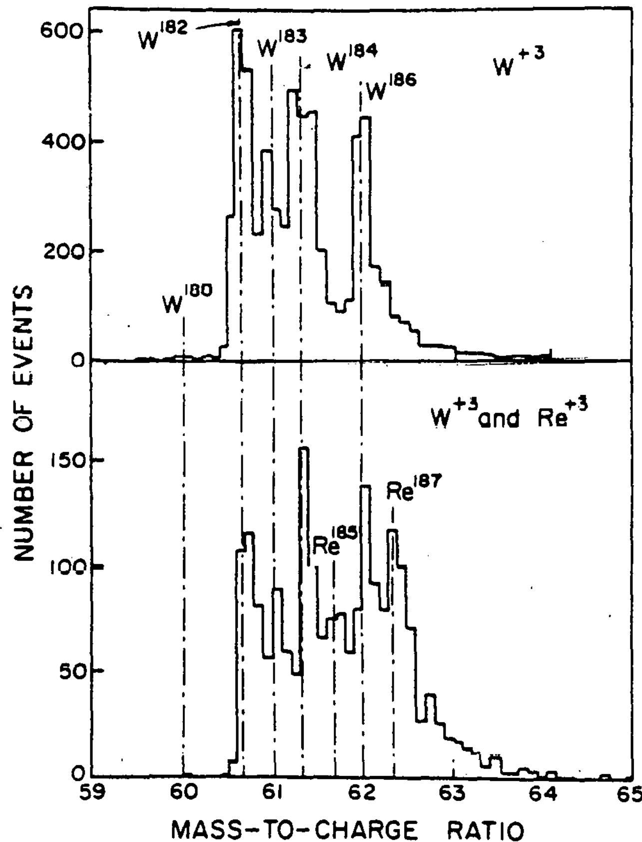

Fig. 3a The W^{+3} spectrum of Westinghouse as-received tungsten pulse-field evaporated at 25 K with f=0.05 for V_{dc} varied continuously from 13 to 15 kV. The ions were collected from the (551) plane and the background pressure in the atom probe was 6×10^{-10} Torr. The calibration parameters used were $\alpha=2.0$, $t_o=0.56\mu$sec and d=1.6003 m. The total number of W^{+3} events in this histogram is 6045.

Fig. 3b The W^{+3} and Re^{+3} spectrum of W-25 at.% Re thermocouple wire. The spectrum was recorded at a specimen temperature of ≈25 K with a f=0.10 at a pressure of 5×10^{-9} Torr. The calibration parameters used were $\alpha=1.5$, $t_o=0.56\mu$sec and d=2.232 m. The total number of W^{+3} and Re^{+3} events in this histogram is 1755.

A Catalogue of Applications to the Study of Defects, Radiation Damage and Implanted Gases in Solids

In this section we present, in catalogue form, a list of problems to which we have applied the FIM and atom probe techniques. The reader is referred to the references for the details concerning each problem.

Diffusive Properties of Self-Interstitial Atoms (SIAs)

a. Measured enthalpy change of migration (Δh_{1i}^{m}) of SIAs in pure metals, alloys and order-disorder alloys.

b. Measured the pre-exponential factor (D_{1i}^{o}) of the SIA self-diffusion coefficient.

c. Have studied SIAs in the recovery stages I, II and III of ion, electron or fast-neutron irradiated specimens.

d. The particular systems studied to date are W, W(Re), W(C), Mo, Pt, Pt(Au), Ni_4Mo and Pt_3Co.

e. For details see reference numbers (18, 19, 21, 27-40).

Volume Change of Migration (Δv_{1i}^{m}) of SIAs

a. Measured Δv_{1i}^{m} for the SIA in W, Pt and Mo in detail. Experiments were also performed on Ni_4Mo and Pt_3Co but in less detail.

b. For further details see reference numbers (18, 19, 27, 28, 31, 37-41).

Binding Enthalpy of an SIA to a Solute Atom (Δh^{b})

a. Measured Δh^{b} by determining a dissociation enthalpy (Δh^{d}) and then determining Δh^{b} from the expression $\Delta h^{d} = \Delta h^{b} + \Delta h_{1i}^{m}$. The system Pt(Au) was studied in great detail and two thermally activated detrapping stages (II_B and II_C) were observed in Stage II.

b. The systems W(Re) and W(C) were also studied but in less detail.

c. For further details see reference numbers (19, 21, 36, 39, 40).

Diffusive Properties of Vacancies

a. Measured ratio of divacancy concentration to monovacancy concentration for one quench temperature in platinum specimens.

b. From (a) it was possible to determine the Gibbs free binding energy of a divacancy (Δg_{2v}^{b}) in platinum for one quench temperature.

c. Measured vacancy concentration in tungsten specimens which had been quenched from near the melting point.

d. The measurements discussed in (a) to (c) are important for the interpretation of the high-temperature self-diffusion data in terms of point-defect mechanisms.

e. For further details see reference numbers (18, 42-46).

Diffusive Properties of Gases in Metals

a. Diffusion of ^{3}He and ^{4}He in tungsten.

b. Diffusion of ^{1}H in tungsten.

c. For further details see reference numbers (47-51).

Range Profiles of Low-Energy Implanted Gases in Metals

a. Range profiles of ^{3}He and ^{4}He in tungsten (100 to 1500 eV singly-charged ions).

b. Range profiles of ^{1}H in tungsten.

c. For further details see reference numbers (47-53).

Point-Defect Structure of Depleted Zones: The Primary State of Radiation Damage

a. Depleted zones in ion-irradiated metals [W, Pt, Pt(Au)]

   (i) Dimensions of depleted zones (DZs).

   (ii) Number of vacancies per DZ.

   (iii) Vacancy concentration within a DZ.

   (iv) The distribution of first-nearest-neighbor vacancy clusters within a DZ.

   (v) The radial distribution function for the vacancies within a DZ, out to ninth-nearest-neighbor.

b. Effect of projectile mass (M_1) on the vacancy structure of DZs at constant projectile energy (E_1).

c. Effect of E_1 — at constant M_1 — on the vacancy structure of DZs.

d. For further details see reference numbers (18, 20, 21, 49, 54-62).

Radiation Damage Profiles

a. Radiation damage profiles were measured in tungsten and platinum by determining the positions of all the vacancies, contained within DZs, as a function of distance from the irradiated surface.

b. Direct determination of radiation damage profiles in order-disorder alloys. After an irradiation each specimen was dissected on an atom-by-atom basis and the change in the Bragg-Williams long-range order parameter was determined as a function of distance from the irradiated surface. This approach was applied in great detail to Pt_3Co, which had been irradiated with 250 to 2500 eV Ne^+ ions, and in less detail to Ni_4Mo.

c. For further details see reference numbers (38, 49, 59, 60).

Sputtering of Surfaces

a. The sputtering of a metal surface is the result of the intersection of a collision cascade with the surface. In this work we compared the vacancy structure of DZs, produced by 30 keV W^+, Mo^+, Cr^+, Cu^+ or Ar^+ ions, that were found to have intersected the surface of a tungsten FIM specimen with those found in the bulk of the specimen.

b. For further details see reference numbers (64, 65).

Voids in Neutron-Irradiated Metals [Mo, Mo(Ti), Fe(Cu)]

a. Void number density: need a number density of $\approx 10^{17} cm^{-3}$ in order to be able to make measurements.

b. Void size distribution: same comment as above is applicable.

c. Direct observation of segregation of alloying elements.

d. For further details see reference numbers (66-68).

Distribution of SIAs in the Primary Damage State

a. The distribution of SIAs was determined in tungsten which had been ion irradiated at 10 K — below the Stage I recovery peaks — with 18 keV Au^+, 20 keV W^+ or 30 keV Cr^+ ions along high index crystallographic directions.

b. From the distribution of SIAs we were able to place upper limits on the ranges of focused replacement collision sequences in tungsten.

c. For further details see reference numbers (54,69).

Range Profiles of Low-Energy (100 to 1500 eV) Implanted ^{3}He and ^{4}He Atoms and the Diffusivity of ^{3}He and ^{4}He in Tungsten

General Background

Current interest in the fundamental properties of helium in metals has been generated by the materials problems associated with the development of the liquid-metal fast-breeder reactor (70) and the controlled thermonuclear reactor (71). However, because of a lack of appropriate experimental techniques the investigations of the range of low-energy (<1 keV) implanted helium atoms and the diffusivity of He in metals have been largely theoretical (72-74). Measurement of the range profiles of implanted He ions have been confined to energies (75) >1 keV; furthermore, the measurement of both the range profiles of implanted He and the diffusivity of He in metals have relied exclusively on the trapping of He at lattice defects introduced as a result of heavy-ion irradiation (76).

The accomplishments of our research on helium implanted in tungsten were: (1) the establishment of the ability of the atom-probe FIM to detect either implanted ^{3}He or ^{4}He atoms retained in a perfect (i.e., totally defect-free) lattice; (2) the detection of the presence of an isolated and immobile ^{3}He or ^{4}He atom in a perfect tungsten lattice; (3) the measurement of the range profiles of low-energy (100 to 1500 eV) implanted ^{3}He or ^{4}He atoms in a tungsten lattice; and (4) the measurement of the diffusivities of ^{3}He and ^{4}He in a perfect tungsten lattice.

The basic physical ideas involved in the experimental procedures are illustrated sequentially in Figure 4. A single-crystal tungsten FIM specimen, at an irradiation temperature (T_i), was irradiated **in situ** with $^{3}He^{+}$ or $^{4}He^{+}$ ions parallel to the [110] direction as shown in Figure 4(a). To study the diffusional behavior of either ^{3}He or ^{4}He in tungsten it was necessary to implant the helium under the condition of **no** radiation damage. For example, a 300-eV ^{4}He atom can transfer a maximum energy of $\sim$ 25 eV to a tungsten W atom in a head-on two-body elastic collision. Since the minimum displacement energy for the production of a stable Frenkel pair in tungsten is $\approx$42 eV (77), no self-interstitial atoms (SIAs) or vacancies were created at an implantation energy of 300 eV for either ^{3}He or ^{4}He. Thus for the diffusion experiments a standard implantation energy of 300 eV was employed. With no SIAs or vacancies present to act as trapping centers, implanted ^{3}He or ^{4}He atoms can remain in the specimen **only** if ^{3}He or ^{4}He is immobile at T_i. Thus, the state of the tungsten specimen after an implantation consisted of immobile interstitial ^{3}He or ^{4}He atoms implanted in a perfect tungsten lattice with a depth distribution that was determined solely by the range profile of the low-energy ions. Next the specimen was analyzed chemically, by the atom-probe technique, at a standard reference temperature (T_r), where $T_r \leq T_i$, and a ^{3}He or ^{4}He integral profile was plotted as shown in Figure 4(b); this was an integral profile since it measured the cumulative number of ^{3}He or ^{4}He atoms as a function of the cumulative number of tungsten atoms (depth) from the irradiated surface. The depth scale was converted from cumulative number of tungsten atoms to angstroms from the measured number of tungsten atoms per (110) plane contained within the cylindrical element sampled; see Figure 4(a). Finally the ^{3}He or ^{4}He range profile, Figure 4(c), can be constructed by taking the first derivative of the integral profile shown in Figure 4(b); or alternatively by plotting a frequency distribution diagram.

A novel technique for the determination of an absolute depth scale was developed; Figure 5 schematically illustrates the method. During the atom-probe analysis the specimen was oriented and the magnification adjusted so that only the central portion of the (110) plane of the tungsten specimen was chemically analyzed. The specimen was then pulse field evaporated through the repeated application of high-voltage pulses. Three successive stages in the pulse field evaporation of one (110) plane are indicated in Figure 5(a). As the specimen was pulsed, field-evaporated ions were detected as indicated by the positive slope in Figure 5(b). When a plane completely evaporated the slope of the curve in Figure 5(b) returned to zero. Therefore the removal of one (110) plane resulted in a single-step increase in the plot of the number of tungsten atoms detected versus the number of field-evaporation pulses applied to the specimen. Since the tungsten lattice was employed as a depth marker, the absolute depth of each implanted ^{3}He or ^{4}He atom from the initial irradiated surface was measured to within one (110) interplanar spacing ($\approx$ 2.24Å) **independent** of the total depth of analysis. Thus the spatial depth resolution of the atom-probe technique is limited solely by the interplanar spacing of the region being analyzed.

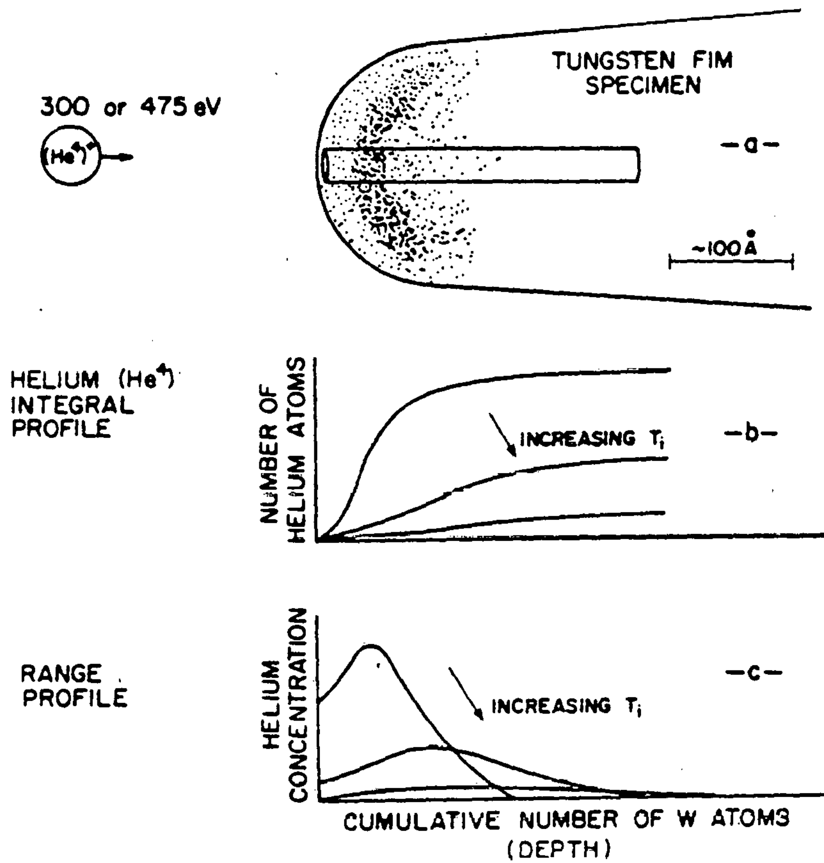

Fig. 4 (a) The *in situ* irradiation of a tungsten FIM specimen with 300 eV $^4He^+$ ions at a T_i where the implanted ^4He atoms are immobile. The density of spots corresponds to the approximate range profile of ^4He in tungsten. The cylindrical volume element represents the volume chemically analyzed by the atom probe technique. (b) The cumulative number of ^4He atoms versus depth as a function of T_i. Note that the ^4He integral profile tends to flatten out as a T_i is increased. (c) The range profiles of ^4He in tungsten as a function of T_i. The same concepts illustrated here for ^4He apply, of course, to ^3He.

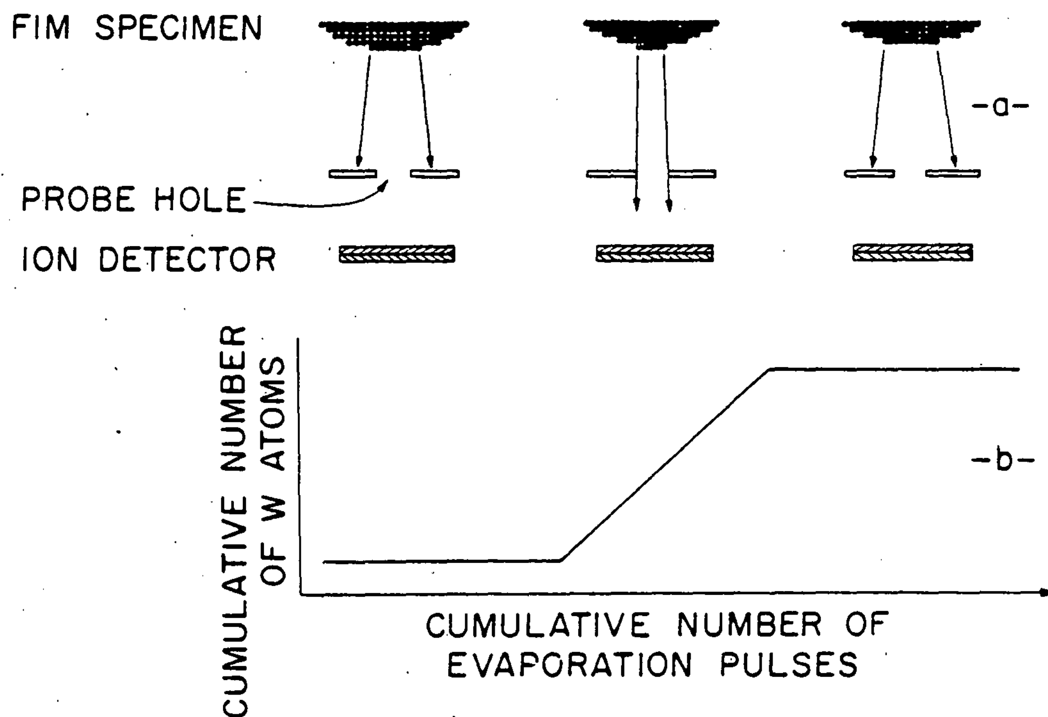

Fig. 5. A schematic diagram illustrating the method employed to determine an absolute depth scale. Three states in the field evaporation of one (110) plane of tungsten W are shown in (a). The field-evaporation behavior of this plane is indicated in (b) by the steplike increase in the rate at which tungsten atoms are detected.

Integral and range profiles of low-energy implanted ^{3}He and ^{4}He atoms

In this section we present a number of integral profiles and range profiles for both ^{3}He and ^{4}He which had been implanted in tungsten at 60 K. The term integral profile reflects the manner in which the data was recorded [see Figure 4(b)], whereas the range profile was constructed by plotting a frequency distribution diagram from the integral profile [see Figure 4(c)]. The range profile can also be obtained by drawing a smooth curve through the integral profile and taking the first derivative of this curve. In all cases we have obtained the range profile by the former rather than the latter technique.

Figure 6 exhibits ^{3}He integral profiles for the implantation energies 100, 500 and 1500 eV; the 100 eV profile is a composite of two integral profiles, each at a dose of 4.7×10^{15}ions cm^{-2}; both the 500 and 1500 eV integral profiles were obtained after implanting to a dose of 3×10^{15}ions cm^{-2}. In Figure 7 we show a composite range profile for 300 eV ^{3}He ions; this range profile was constructed from seven integral profiles and includes a total of 385 ^{3}He events; the values of the mean range ($\bar{x}$) and the straggling (Δx) are 54.9 and 41.5 Å, respectively.

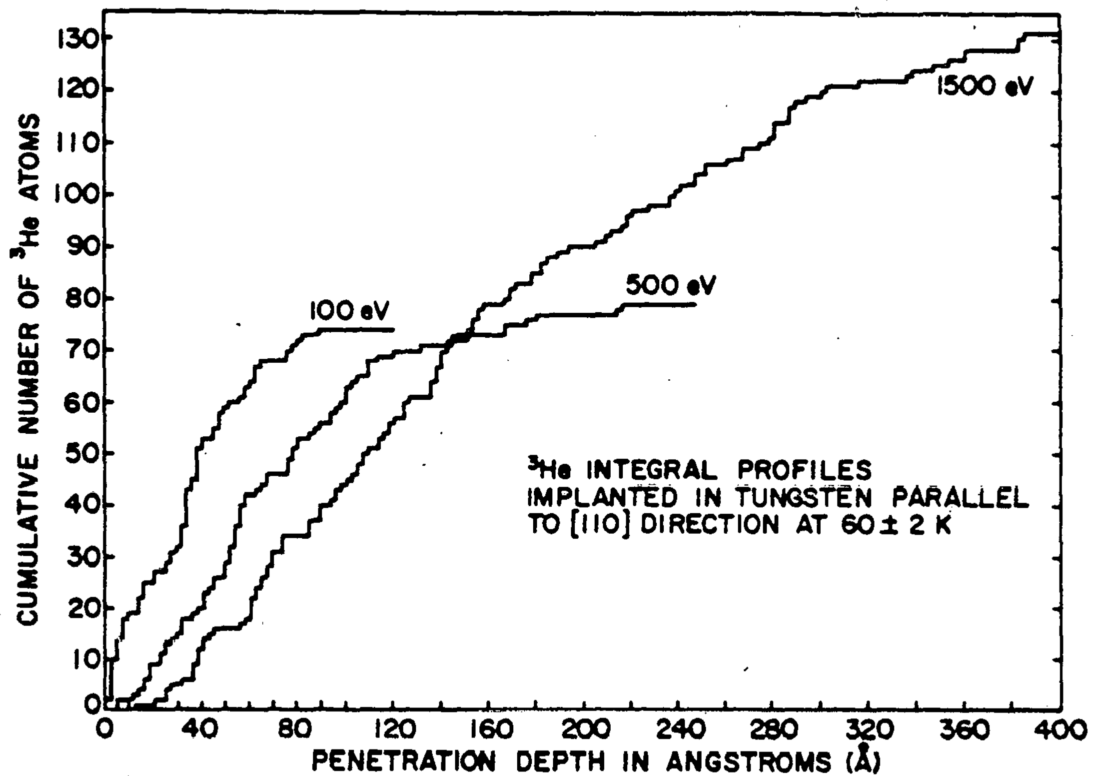

Fig. 6. The ^{3}He integral profiles for the implantation energies of 100, 500 and 1500 eV. The tungsten specimens were implanted at 60 K parallel to the [110] direction.

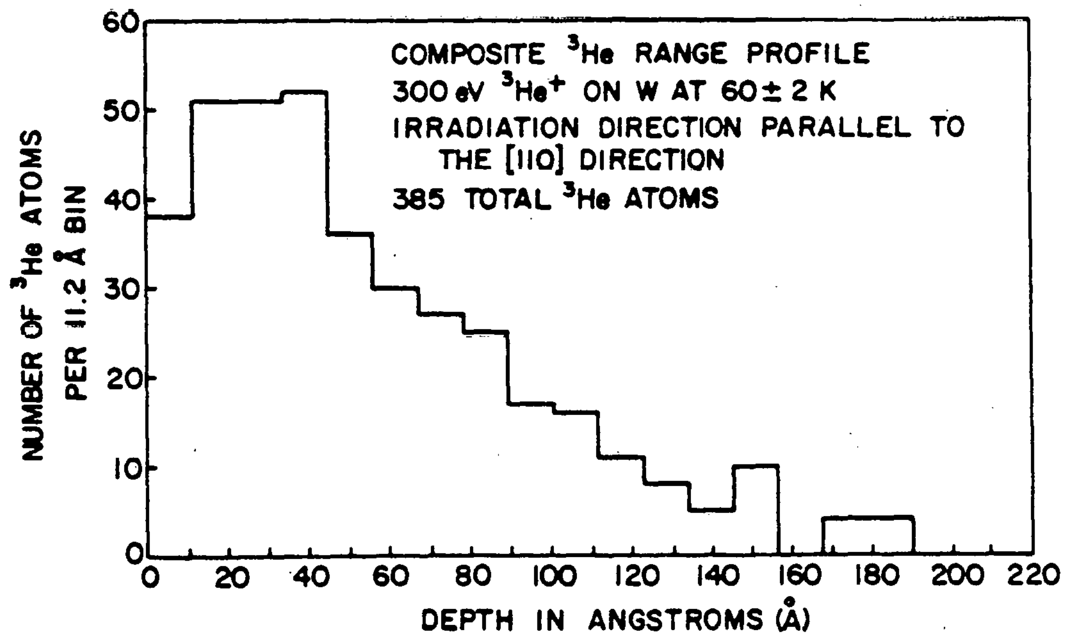

Fig. 7. A composite ^{3}He range profile for all the 300 eV implantations at 60 K. A total of 385 ^{3}He events were involved in the construction of this range profile.

Figure 8 exhibits ^{4}He integral profiles for the implantation energies 150, 500 and 1000 eV; the 150 eV data consists of a single integral profile for a specimen that had been implanted to a dose of 3×10^{15} ions cm^{-2}; the 1000 eV data is for a single integral profile for a specimen that had received a dose of 4×10^{15} ions cm^{-2}. In Figure 9 we show a composite range profile for a 1000 eV ^{4}He implantation; this range profile was constructed from three integral range profiles and includes a total of 147 ^{4}He events; the values of $\bar{x}$ and Δx are 133 and 104.2 Å, respectively.

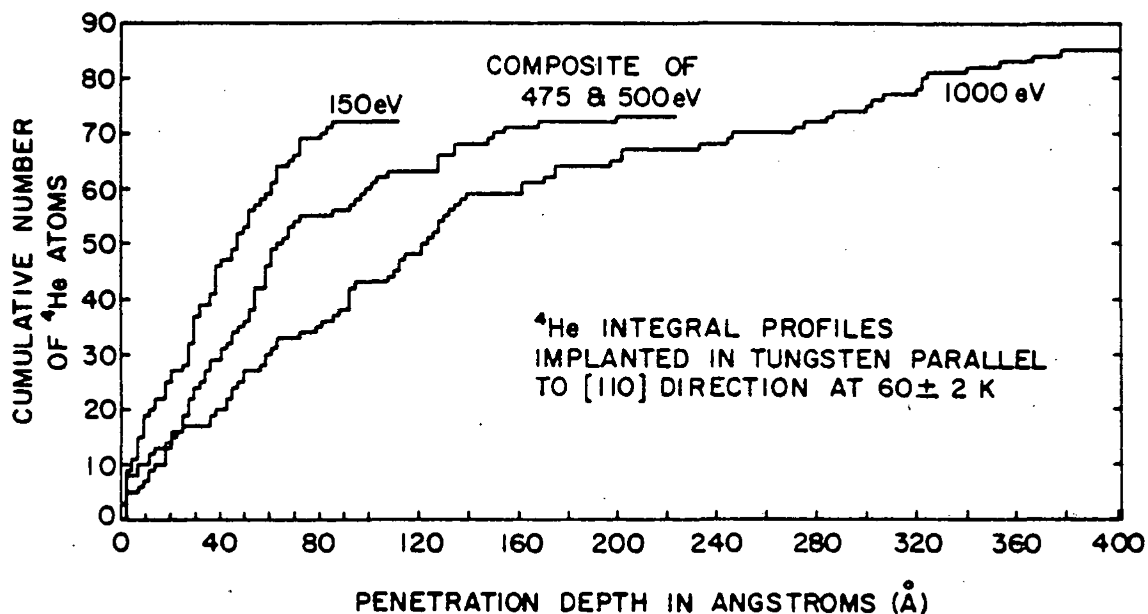

Fig. 8. The ^{4}He integral profiles for the implantation energies of 150, (475 and 500), and 1000 eV. The tungsten specimens were implanted at 60 K parallel to the [110] direction.

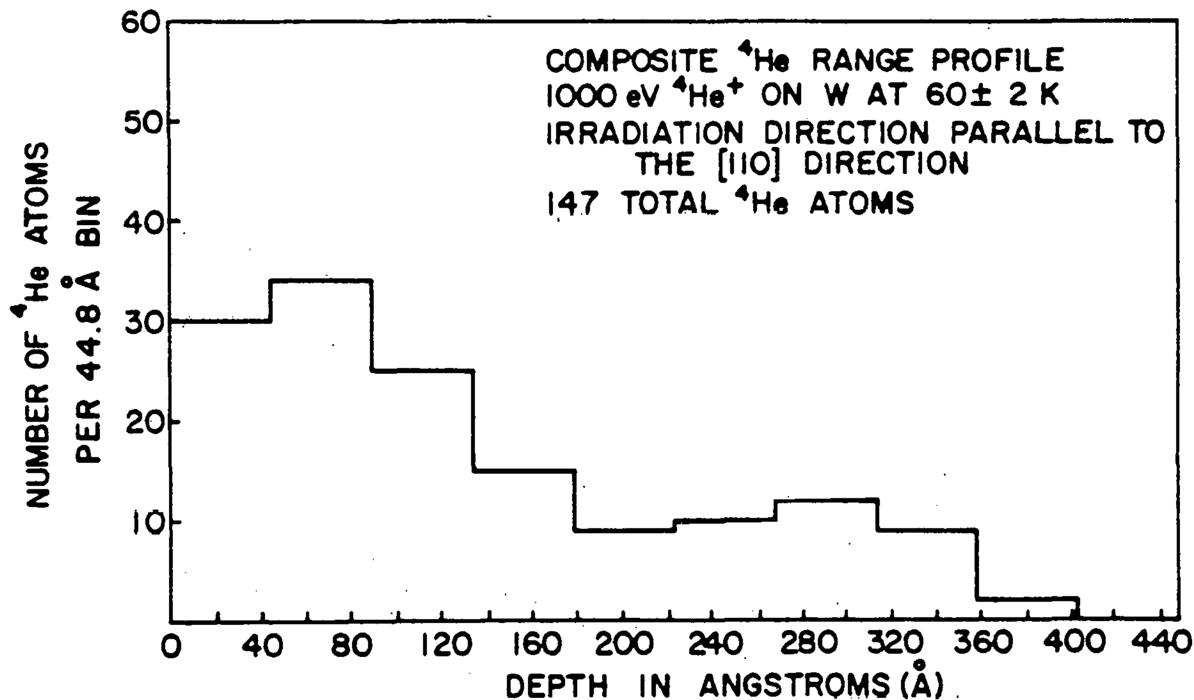

Fig. 9. A composite ^{4}He range profile for all the 1000 eV implantations at 60 K. A total of 147 ^{4}He events were recorded in the construction of this range profile.

All of the ^{3}He and ^{4}He integral profiles exhibited positive skewness as expected for low-energy irradiations [Biersack and Haggmark (78)]; this implied that the mean range ($\bar{x}$) was greater than the most probable range (or mode) and that the majority of the large deviations were to the right (positive) side of $\bar{x}$. The coefficient of skewness is related to the third moment about $\bar{x}$ and is given [Parratt (79)] by:

$$\text{Coefficient of Skewness} = \frac{\sum_{i=1}^{N}(x_i - \bar{x})^3}{N(\Delta x)^3}; \quad (1)$$

where x_i is the measured depth of the ith detected helium atom from the initial irradiated surface, N is the total number of helium events detected and Δx is the standard deviation or straggling.

The values of $\bar{x}$ and Δx were calculated directly from the integral profiles for the ^{3}He and ^{4}He implantations. The values $\bar{x}$ and Δx were referred to as uncorrected quantities. The reason for this is that $\bar{x}$ and Δx must be corrected for the following systematic errors: (1) the random arrival of helium atoms at the surface of the specimen, from the residual partial pressure of helium, during the atom-probe analysis of the irradiated specimen; and (2) the effect of the finite curvature of the FIM specimen. A detailed analysis of the above effects is given elsewhere [Amano, Wagner and Seidman (52,53)], where it was shown that the corrections to $\bar{x}$ and Δx were very minimal in our experiments. Thus we shall not employ the word uncorrected any further in this paper.

Figure 10 exhibits $\bar{x}$ (in Å) versus the incident ion energy (in eV) for both the ^{3}He (solid black circles) and the ^{4}He (open circles) implantations. The total length of each error bar is two standard deviations in the mean (Δx_m), i.e., plus or minus one Δx_m. The quantity Δx_m is given by:

$$\Delta x_m = \Delta x/\sqrt{N}, \quad (2)$$

where N was the total number of helium events detected at a particular incident ion energy for the composite profile. Figure 10 clearly shows that the quantity Δx_m was negligibly small when N exceeded 50 events. The smallest sample size was for the 100 eV ^{4}He implantation where N was equal to 21 events. In this case Δx_m was 3.5Å and the fractional standard error ($\Delta x_m/\bar{x}$) was

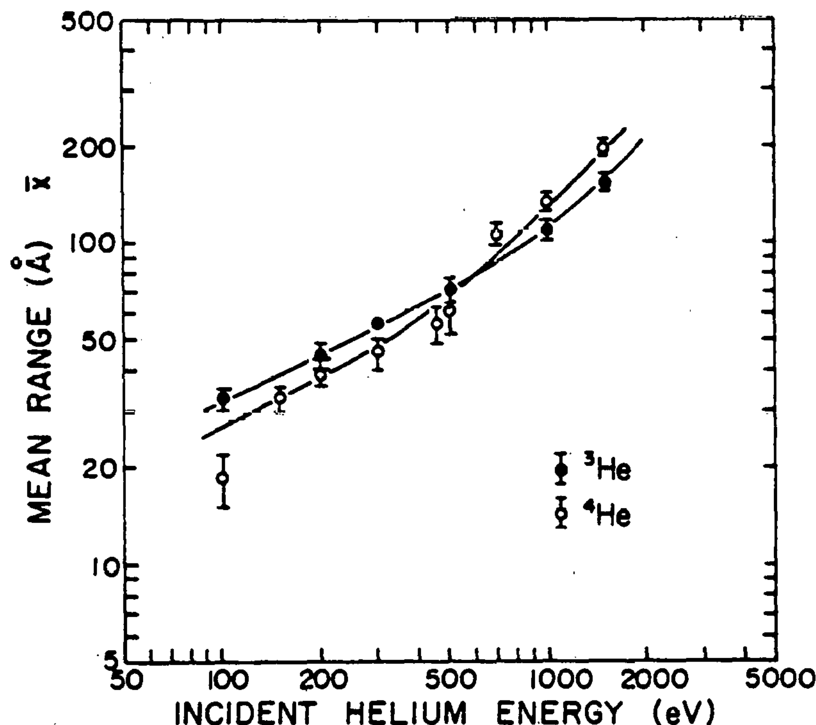

Fig. 10. The mean range ($\bar{x}$) in angstroms versus the incident helium energy (eV) for all the ^{3}He and ^{4}He implantations in tungsten at 60 K.

~0.19. This was the only data point that laid slightly below the smooth line that passes through all the other data points for the ^4He implantations.

The results presented in Figure 10 show that $\bar{x}$ for both ^3He and ^4He increased monotonically, although not linearly, with increasing incident helium ion energy. Overall, for both ^3He and ^4He, the value of $\bar{x}$ increased from 18.7 to 194.9Å as the incident ion energy was increased from 100 to 1500 eV. For an incident helium ion energy of less than 600 eV the $\bar{x}$'s for ^3He were greater than the $\bar{x}$'s for ^4He; this indicated that ^3He penetrated more deeply into the lattice, on the average, than ^4He. At incident helium ion energies greater than 600 eV the $\bar{x}$'s for ^4He exceeded the $\bar{x}$'s for ^3He. A detailed discussion of these effects is given elsewhere [Amano, Wagner and Seidman (52,53)].

Figure 11 displays Δx as a function of the incident helium ion energy for both ^3He and ^4He; Δx is very commonly known as the straggling, since it determines the width of the range profile. The length of each error bar in figure 11 is equal to two universe standard deviations in the sample standard deviation (Δx_s), i.e., plus or minus one Δx_s. The quantity Δx_s, for a normal distribution, is given by [Parratt (79)]

$$\Delta x_s = \Delta x/\sqrt{2N}. \quad (3)$$

We have used Eqn. (3) to obtain approximate values of Δx_s for our range profiles, which are actually skewed from a normal distribution. It is seen from Figure 11 that for the sample sizes we employed the values of Δx_s were all rather small.

For both ^3He and ^4He the value of Δx increased monotonically, although **not** linearly, with increasing incident helium ion energy (see Figure 11). The quantity Δx ranged from 16 to 124 Å as the incident helium ion energy was increased from 100 to 1500 eV. At an incident helium ion energy of ~300 eV the two curves crossed one another and the Δx's for ^4He were greater than those for ^3He. This indicated that as the incident ion energy was increased the ^4He was distributed in space, both wider and deeper than ^3He.

Figure 12 exhibits the relative variance $[(\Delta x)^2/(\bar{x})^2]$ of the ^3He and ^4He range profiles, as a function of the incident helium ion energy (in eV). Within the scatter of the data the quantity $(\Delta x)^2/(\bar{x})^2$ for ^3He exhibited a constant value of ~0.47 and the same quantity for ^4He was ~0.61. Thus in the energy range 100 to 1500 eV the value of $(\Delta x)^2/(\bar{x})^2$ for ^4He was greater than for ^3He. This clearly indicated that the ^4He was distributed more broadly in space than was the ^3He.

Detection of possible radiation damage in the case of the 300 eV helium implantations

In order to establish that the ^4He detected in the case of the 300 eV implantation experiment was **not** trapped at structural defects in the tungsten lattice, the following isochronal recovery experiment was performed. A tungsten specimen was irradiated along the [110] direction with 300-eV $^4He^+$ ions at ~30 K. After the irradiation ≈ two (110) planes, corresponding to ≈4.48 Å of material, were pulse field evaporated from the specimen. This procedure removed the sputtered surface and restored the surface to a nearly perfect state. The specimen was then warmed isochronally from ≈30 to 90 K at a rate of 1.5 K min^{-1}, while the FIM image was photographed at a rate of two 35-mm cine frames sec^{-1}. No SIA contrast effects were observed during this experiment, indicating that **no** SIA crossed the surface of the FIM specimen.† Our previous work (80) demonstrated that if SIAs were present they would have appeared throughout the entire range of 38 to 90

† Helium atoms do not give rise to visible contrast effects in the FIM image, thus this type of experiment can not be used to detect the recovery behavior of interstitial helium atoms. Note, however, that the depth profiling experiments demonstrated that helium does **not** become mobile until 90 K.

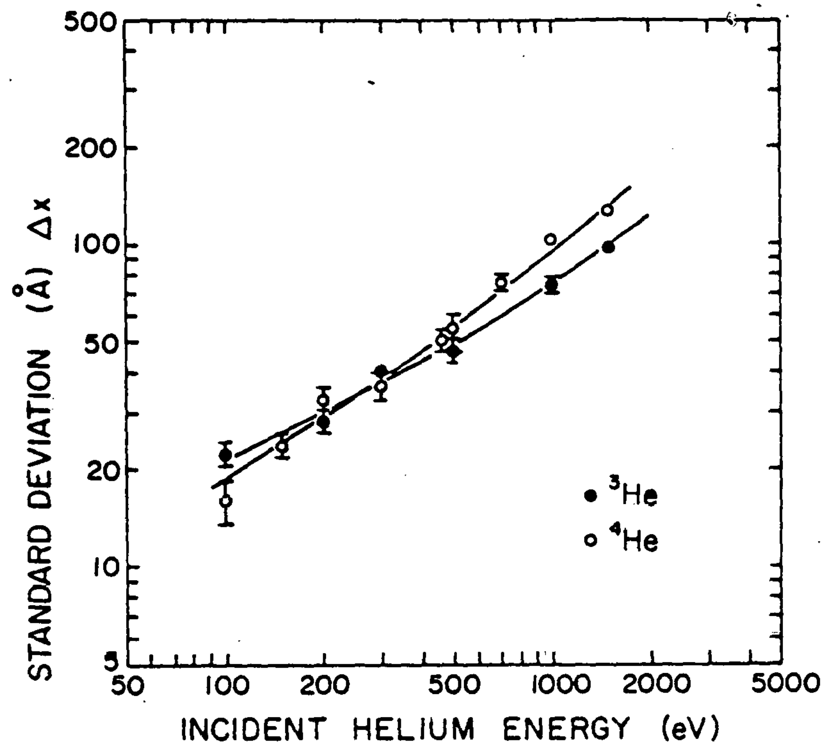

Fig. 11. The standard deviation or straggling in angstroms (Δx) versus the incident helium energy (eV) for all the ^{3}He and ^{4}He implantations in tungsten at 60 K.

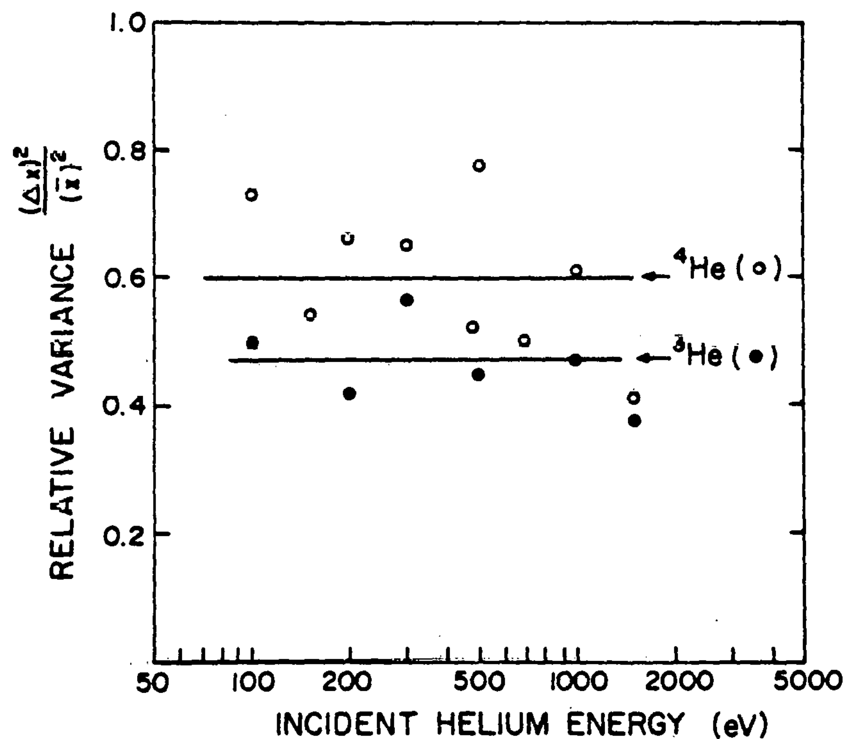

Fig. 12. The relative variance $[(\Delta x)^2/(\bar{x})^2]$ versus the incident helium energy (eV) for all the ^{3}He and ^{4}He implantations in tungsten at 60 K.

K. The specimen was then dissected by the pulse field evaporation technique and was examined for point defects. The density of point defects was determined to be $<8\times10^{-4}$ (atomic fraction); their depth distribution was not related to the ^{4}He integral profiles. These results constitute conclusive evidence that the ^{4}He was **not** trapped at SIAs or vacancies. This indicated that the ^{4}He atoms were located in the interstices of the lattice and that they were immobile in tungsten at 60 K.

The diffusivities of ^{3}He and ^{4}He in tungsten

The temperature at which the interstitial ^{4}He (or ^{3}He) atoms became mobile in tungsten was determined by implanting ^{4}He (or ^{3}He) in an FIM specimen at different T_i's and then analyzing at T_r=60 K. The ^{4}He (or ^{3}He) integral profile determined at T_r was independent of T_i only if the ^{4}He (or ^{3}He) was immobile at all values of T_i. However, when T_i was above the temperature at which the ^{4}He (or ^{3}He) interstitials became mobile, the ^{4}He (or ^{3}He) implanted during the irradiation diffused to the surface of the FIM specimen and entered the gas phase. Therefore a sharp decrease in the measured ^{4}He (or ^{3}He) concentration was expected as T_i was increased [see Figure 4(c)]. Since only T_i was varied, significant changes in the integral profile could only be attributed to a sharp increase in the mobility of the interstitial ^{4}He (or ^{3}He) atoms at T_i. A dramatic change in the integral profile was observed upon increasing T_i from 90 to 110 K; thus indicating that interstitial ^{4}He or (^{3}He) atoms were immobile at 90 K but were highly mobile at 110 K. By employing a diffusion model, a value of the enthalpy change of migration ($\Delta h^m_{^4He}$) of 0.24 to 0.32 eV was estimated (47,48). The upper and lower limits on $\Delta h_{^4He}$ were determined by the values of the pre-exponential factor (D_o) chosen for the diffusion model and by the uncertainty in the diffusion temperature, i.e., 90 to 110 K; the lower limit was determined by a D_o of 1×10^{-3} cm sec^{-1} and a T of 90 K and the upper limit by a D_o of 1×10^{-2} cm^2 sec^{-1} and a T of 110 K. The uncertainty in $\Delta h^m_{^4He}$ was divided approximately equally between the uncertainty in D_o and T.

The diffusivity of ^{3}He in tungsten was determined by actually following the isothermal recovery of 300 eV implantation profiles which had been implanted at 90, 95, 98, 100 and 110 K. The diffusion equation was solved with appropriate initial and boundary conditions, to describe the diffusion of ^{3}He out of an FIM tip under isothermal conditions. The fit of the experimental isothermal recovery data to the solution of the diffusion equation yielded the diffusivity of ^{3}He as a function of temperature. The results of this work are shown in Figure 13. It is seen that the data is best described by the expression

$$D(^3He) = (5.4 \pm {}^{10.6}_{3.8})\times10^{-3} \exp[\frac{-0.28 \text{ eV}}{kT}] cm^2 sec^{-1}.$$

Thus within the measured experimental uncertainties the Δh's for ^{3}He and ^{4}He in tungsten are identical. For further details on the diffusivity of ^{3}He in tungsten see Amano and Seidman (51).

Conclusions

The field-ion and atom-probe field-ion microscopes are ideally suited for studying a wide range of fundamental problems, concerning point defects in irradiated or quenched metals, that require information on an atomic scale. The atom-probe field-ion-microscope with its ability to measure the mass-to-charge ratio of a single ion can be brought to bear on problems that need chemical information on an angstrom scale. Since the atom-probe field-ion microscope is essentially a field-ion microscope coupled to a special time-of-flight mass spectrometer the main features of both instruments are contained in the atom probe. Thus, it is now possible to both image the microstructural features, with atomic resolution, of a specimen and to subsequently measure the mass-to-charge ratio of individual ions from these microstructural features, with a lateral spatial resolution (i.e., within the surface) of a few angstroms and a depth resolution that is determined by the interplanar spacing; the latter quantity can be tenths of an angstrom for a high index plane.

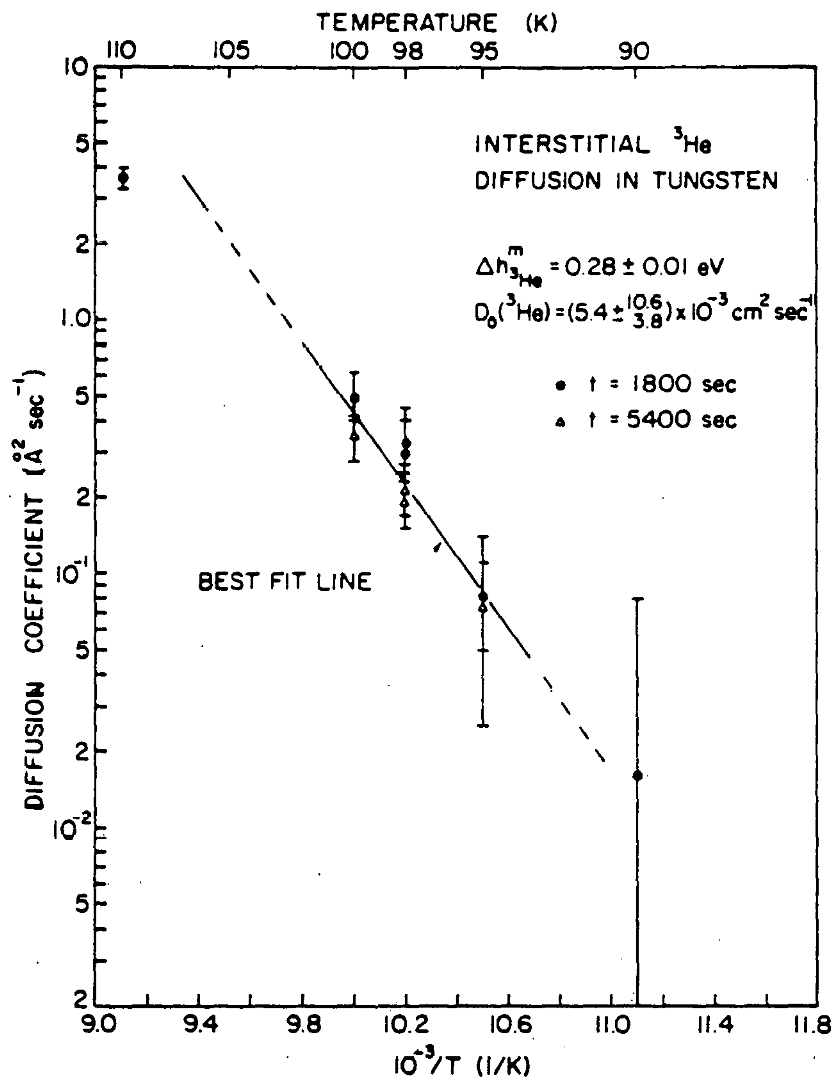

Fig. 13. The diffusion coefficient of ^{3}He versus (1/T) in the temperature range 90 to 110 K. The times indicated (1800 and 5400 sec) correspond to different recovery times at each temperature. Note that 1Å^{2}sec^{-1} is equal to 10^{-16}cm^2 sec^{-1}.

The principal shortcoming of the atom probe field-ion microscope is that only the more refractory metals and alloys have so far been routinely easily studied. Thus, to date, our own studies have focused heavily on the pure metals tungsten, molybdenum and platinum; the alloys tungsten (rhenium), tungsten (carbon), platinum (gold) and molybdenum (titanium), and the order-disorder alloys Ni_4Mo and Pt_3Co. This is not meant to imply that other pure metals or alloy systems are not amenable to the technique, but rather that they were the ones which we found easiest to work on in order to study certain specific physical problems. For example, it was possible to chemically analyze, on a quantitative basis, both an alloy as complex as stainless steel and a quaternary metallic glass (Metglas 2826) (24). The application of the atom-probe field-ion microscope to the study of clustering and precipitation in some reasonably complex alloys has been reviewed recently by Brenner (81) and the reader is referred to his paper for details. The atom-probe field-ion microscope could also be used to study the structure of metallic glasses as has been suggested recently by Jacobaeus *et al.* (82).

This paper, first, briefly reviewed the physical basis of the field-ion and atom-probe microscope techniques (see the section entitled **General Background Material**). Second we presented, in catalogue form, a list of the problems to which we have applied the field-ion microscope and atom probe techniques. This section contains many references to the original papers, so that the reader can follow his own research needs in detail. Finally, a presentation was made of our recent results on the behavior of ^3He and ^4He atoms implanted in tungsten, employing the atom-probe field-ion microscope technique. The range profiles of low-energy (100 to 1500 eV) ^3He and ^4He atoms implanted in tungsten, at 60 K, were measured with a depth resolution of one (110) interplanar spacing (2.24Å). At 60 K both ^3He and ^4He were found to be immobile. Thus, the range profiles were determined in the complete absence of any diffusional effects. All of the ^3He and ^4He range profiles exhibited positive skewness. Both ^3He and ^4He were found to be highly mobile in the temperature range 90 to 110 K. Experiments were described that measured, for the first time, the diffusivities of ^3He and ^4He atoms in the absence of any defects — i.e., in a perfect crystal lattice — in this temperature range.

Acknowledgements

We wish to thank Dr. S. S. Brenner for many useful discussions over the years concerning the field-ion and atom-probe microscope techniques and Mr. R. Whitmarsh for enthusiastic technical assistance in all phases of the experimental program.

References

1. E. W. Müller, Z. Physik *131*, 136 (1951).
2. E. W. Müller, J. A. Panitz and S. B. McLane, Rev. Sci. Instrum. *39*, 83 (1968).
3. P. J. Turner, P. Cartwright, M. J. Southon, A. van Oostrom and B. W. Manley, J. Sci. Instrum. *2*, 731 (1969).
4. S. S. Brenner and J. T. McKinney, Surface Sci. *23*, 88 (1970).
5. E. W. Müller and T. T. Tsong, *Field-Ion Microscopy* (American Elsevier, New York, 1969), Chapt. II.
6. E. W. Müller and T. T. Tsong, *Field-Ion Microscopy* (American Elsevier, New York, 1969), Chapt. III.
7. R. M. Scanlan, D. L. Styris, D. N. Seidman and D. G. Ast, Cornell Materials Science Center Report No. 1159 (1969).
8. W. P. Poschenrieder, Int. J. Mass Spectrom. and Ion Phys. *9*, 357 (1972).
9. E. W. Müller and S. V. Krishnaswamy, Rev. Sci. Instrum. *45*, 1053 (1974).
10. R. Gomer, *Field Emission and Field-Ionization* (Harvard University Press, Cambridge, Massachusetts, 1961).

11. *Field-Ion Microscopy*, edited by J. J. Hren and S. Ranganathan (Plenum Press, New York, 1968).
12. *Applications of Field-Ion Microscopy*, edited by R. F. Hochman, E. W. Müller and B. Ralph (Advanced Research Projects Agency, ARPA order No. 878 and the Georgia Institute of Technology, 1969).
13. K. M. Bowkett and D. A. Smith, *Field-Ion Microscopy* (American Elsevier, New York, 1970).
14. *Field-Ion, Field Emission Microscopy and Related Topics*, special issue of Surface Sci. *23*, 1 (1970).
15. E. W. Müller and T. T. Tsong, in *Progress in Surface Science*, edited by S. G. Davison (Pergamon Press, Oxford, 1973), Vol. 4, Part I, pp. 1-139.
16. J. A. Panitz, in *Progress in Surface Science*, edited by S. G. Davison (Pergamon Press, Oxford, 1978), Vol. 8, pp. 219-62.
17. *Proceedings of the Int. Symp. on Application of FIM to Metallurgy*, edited by R. R. Hasiguti, Y. Yashiro and N. Igata (Dept. of Metallurgy and Materials Science, Univ. of Tokyo, Tokyo, Japan, 1977); *Proceedings of the 27th International Field Emission Symposium*, edited by Y. Yashiro and N.. Igata (Dept. of Metallurgy and Materials Science, Univ. of Tokyo, Tokyo, Japan, 1980).
18. D. N. Seidman, J. Phys. F: Metal Phys. *3*, 393 (1973).
19. D. N. Seidman, K. L. Wilson and C. H. Nielsen, in *Proceedings of the Int. Conf. on Fundamental Aspects of Radiation Damage in Metals*, edited by M. T. Robinson and F. W. Young, Jr. (National Technical Information Service, U.S. Dept. of Commerce, Springfield, Virginia, 1975), pp. 373-96.
20. D. N. Seidman, in *Radiation Damage in Metals*, edited by N. L. Peterson and S. D. Harkness (American Society for Metals, Metals Park, Ohio, 1976), pp. 28-57.
21. D. N. Seidman, Surface Sci. *70*, 532 (1978).
22. A. Wagner, T. M. Hall and D. N. Seidman, Rev. Sci. Instrum. *4*, 1032 (1975); A. S. Berger, Rev. Sci. Instrum. *44*, 592 (1973).
23. T. M. Hall, A. Wagner, A. S. Berger and D. N. Seidman, Scripta Met. *10*, 485 (1976).
24. T. M. Hall, A. Wagner and D. N. Seidman, J. Phys. E: Sci. Instrum. *10*, 884 (1977).
25. A. Wagner, T. M. Hall and D. N. Seidman, J. Nuc. Mat. *69* & *70*, 532 (1978).
26. A. Wagner, T. M. Hall and D. N. Seidman, Vacuum *28*, 543 (1978).
27. R. M. Scanlan, D. L. Styris and D. N. Seidman, Phil. Mag. *23*, 1439 (1971).
28. R. M. Scanlan, D. L. Styris and D. N. Seidman, Phil. Mag. *23*, 1459 (1971).
29. P. Petroff and D. N. Seidman, Appl. Phys. Lett. *18*, 518 (1971).
30. D. N. Seidman and K. H. Lie, Acta Met. *20*, 1045 (1972).
31. P. Petroff and D. N. Seidman, Acta Met. *21*, 323 (1973).
32. J. T. Robertson, K. L. Wilson and D. N. Seidman, Phil. Mag. *27*, 1417 (1973).
33. D. N. Seidman, K. L. Wilson and C. H. Nielsen, Phys. Rev. Lett. *35*, 1041 (1975).
34. K. L. Wilson and D. N. Seidman, Radiat. Effects *33*, 149 (1977).
35. D. N. Seidman, Scripta Met. *13*, 251 (1979).
36. K. L. Wilson, M. I. Baskes and D. N. Seidman, Acta Met. *28*, 89 (1980).
37. C. H. Nielsen, M. S. Thesis, Cornell University (1977).
38. J. Aidelberg, Ph.D. Thesis, Cornell University (1980).
39. C.-Y. Wei and D. N. Seidman, Radiat. Effects, *32*, 229 (1977).
40. C.-Y. Wei and D. N. Seidman, J. Nuc. Mat *69&70*, 693 (1978).
41. K. L. Wilson and D. N. Seidman, Rad. Effects *27*, 67 (1975).
42. A. S. Berger, D. N. Seidman and R. W. Balluffi, Acta Met *21*, 123 (1973).
43. A. S. Berger, D. N. Seidman and R. W. Balluffi, Acta Met. *21*, 323 (1973).
44. J. Y. Park, H.-C. W. Huang, A. S. Berger, and R. W. Balluffi, in *Defects and Defect Clusters in B.C.C. Metals and Their Alloys*, edited by R. J. Arsenault (University of Maryland, College Park, MD, 1973), Nuclear Metallurgy, Vol. 18, pp. 420-439.
45. J. Y. Park, Ph.D. Thesis, Cornell University (1975).
46. H.-C. W. Huang, Ph.D. Thesis, Cornell University (1975).
47. A. Wagner and D. N. Seidman, Phys. Rev. Lett. *42*, 515 (1979).
48. A. Wagner, Ph.D. Thesis, Cornell University (1978).
49. D. N. Seidman, U.S. Department of Energy Report No. COO-3158-77 (1979).
50. D. N. Seidman, U.S. Department of Energy Report No. COO-3158-87 (1980).

51. J. Amano and D. N. Seidman, Cornell Materials Science Center Report No. 4153 (1980); submitted for publication.
52. J. Amano, A. Wagner and D. N. Seidman, Cornell Materials Science Center Report No. 4107 (1980); submitted for publication.
53. J. Amano, A. Wagner and D. N. Seidman, Cornell Materials Science Center Report No. 4108 (1980); submitted for publication.
54. L. A. Beavan, R. M. Scanlan and D. N. Seidman, Acta Met. *19*, 1339 (1971).
55. K. L. Wilson and D. N. Seidman, in *Defects and Defect Clusters in B.C.C. Metals and Their Alloys*, edited by R. J. Arsenault (University of Maryland, College Park, MD, 1973), Nuclear Metallurgy, Vol. 18, pp. 216-239.
56. C.-Y. Wei and D. N. Seidman, Phil. Mag. A*37*, 257 (1978).
57. C.-Y. Wei, Ph.D. Thesis, Cornell University (1978).
58. C.-Y. Wei and D. N. Seidman, Appl. Phys. Lett *34*, 622 (1979).
59. D. Pramanik, Ph.D. Thesis, Cornell University (1980).
60. D. N. Seidman, M. I. Current, D. Pramanik and C.-Y. Wei, Cornell Materials Science Center Report No. 4278 (1980); accepted for publication in Nuclear Instruments and Methods.
61. C.-Y. Wei, M. I. Current and D. N. Seidman, Cornell Materials Science Center Report No. 4234 (1980); submitted for publication.
62. M. I. Current, C.-Y. Wei and D. N. Seidman, Cornell Materials Science Center Report No. 4309 (1980); submitted for publication.
63. J. Aidelberg and D. N. Seidman, Nucl. Instrum. and Meth *170*, 413 (1980).
64. M. I. Current, C.-Y. Wei and D. N. Seidman, Cornell Materials Science Center Report No. 4193 (1980); to appear in the Philosophical Magazine (1980).
65. M. I. Current and D. N. Seidman, Nucl. Instrum. Meth. *170*, 377 (1980).
66. S. S. Brenner and D. N. Seidman, Radiat. Effects *24*, 73 (1975).
67. S. S. Brenner, R. Wagner and J. Spitznagel, Met. Trans. A*9A*, 1761 (1978).
68. A. Wagner and D. N. Seidman, J. Nuc. Mat. *83*, 48 (1979).
69. C.-Y. Wei and D. N. Seidman, Cornell Materials Science Center Report No. 4088 (1980); accepted for publication in the Philosophical Magazine.
70. *Radiation-Induced Voids in Metals*, edited by J. W. Corbett and L. C. Ianniello (National Technical Information Service, Springfield, Va., 1972).
71. See, for example, J. Nuc. Mater. *53* (1974); *76* (1978); and *77* (1978).
72. W. D. Wilson and C. L. Bisson, Radiat. Effects *22*, 63 (1974).
73. O. S. Oen and M. T. Robinson, Nuc. Instrum. Meth. *132*, 647 (1976).
74. D. J. Reed, Radiat. Effects *31*, 129 (1977).
75. B. Terreault, R. G. St-Jacques, G. Veilleaux, J. G. Martel, J. L'Ecuyer, C. Brassard and C. Cardinal, Can. J. Phys. *56*, 235 (1978).
76. E. V. Kornelsen, Radiat. Effects *13*, 227 (1972); E. V. Kornelsen and A. A. van Gorkum, Nuc. Instrum. Meth *180*, 161 (1980).
77. F. Maury, M. Biget, P. Vajda, A. Lucasson and P. Lucasson, Radiat. Effects *38*, 53 (1978).
78. J. P. Biersack and L. D. Haggmark, submitted to Nuclear Instruments and Methods (1980).
79. L. G. Parratt, *Probability and Experimental Errors in Science* (John Wiley, New York, 1961), Chapt. 2.
80. R. M. Scanlan, D. L. Styris, and D. N. Seidman, Phil. Mag *23*, 1439 (1971); K. L. Wilson and D. N. Seidman, Radiat. Effects *27*, 67 (1975); D. N. Seidman, K. L. Wilson, and C. H. Nielsen, Phys. Rev. Lett. *35*, 1041 (1975); K. L. Wilson, M. I. Baskes, and D. N. Seidman, Acta. Met. *28*, 89 (1980).
81. S. S. Brenner, Surface Sci. *70*, 427 (1978).
82. P. Jacobaeus, J. U. Madsen, F. Kragh and R. M. J. Cotterill, Phil. Mag. B *42*, 11 (1980).